Cross-Shelf and Out-of-Bay Transport Driven by an Open-Ocean Current

YU ZHANG AND JOSEPH PEDLOSKY

Woods Hole Oceanographic Institution, Woods Hole, Massachusetts

GLENN R. FLIERL

Massachusetts Institute of Technology, Cambridge, Massachusetts

ABSTRACT

This paper studies the interaction of an Antarctic Circumpolar Current (ACC)–like wind-driven channel flow with a continental slope and a flat-bottomed bay-shaped shelf near the channel's southern boundary. Interaction between the model ACC and the topography in the second layer induces local changes of the potential vorticity (PV) flux, which further causes the formation of a first-layer PV front near the base of the topography. Located between the ACC and the first-layer slope, the newly formed PV front is constantly perturbed by the ACC and in turn forces the first-layer slope with its own variability in an intermittent but persistent way. The volume transport of the slope water across the first-layer slope edge is mostly directly driven by eddies and meanders of the new front, and its magnitude is similar to the maximum Ekman transport in the channel. Near the bay's opening, the effect of the topographic waves, excited by offshore variability, dominates the cross-isobath exchange and induces a mean clockwise shelf circulation. The waves' propagation is only toward the west and tends to be blocked by the bay's western boundary in the narrow-shelf region. The ensuing wave–coast interaction amplifies the wave amplitude and the cross-shelf transport. Because the interaction only occurs near the western boundary, the shelf water in the west of the bay is more readily carried offshore than that in the east and the mean shelf circulation is also intensified along the bay's western boundary.

1. Introduction

The continental margin of the west Antarctic Peninsula (WAP) is under the strong influence of the Antarctic Circumpolar Current (ACC). Onshore intrusions of the Circumpolar Deep Water (CDW), a relatively warm and nutrient-rich water mass carried by the ACC, prevail over the WAP shelf and within Marguerite Bay. The presence of the CDW maintains the regional hydrography and makes the region especially well suited to support a large population of Antarctic krill, an essential food source for many large, upper-trophic-level predators. In addition to being significant for the ecosystem, the WAP also undergoes the most dramatic warming on the earth (Turner et al. 2006), raising the question of whether this remarkable regional change can influence the circumpolar waters circulating through the world's oceans. In this paper, we study a driving mechanism for the Upper Circumpolar Deep Water (UCDW) intrusion onto the WAP shelf, the interaction between the shelf topography and the ACC that intermittently sheds eddies to induce the cross-isobath exchange.

The intrusion of the UCDW onto the WAP shelf occurs with a frequency as high as four times a month and in the form of small eddy-like structures (Moffat et al. 2009). The actual driving mechanism of the intrusion, however, is still unclear. Simulations in regional models with realistic configurations of bathymetry and forcing fields suggested a close relation between the curvature of the shelf break and the volume of the cross-shelf transport (Dinniman and Klinck 2004) and between the outbreak of the short-duration winds and the intrusion events (Dinniman et al. 2011). Although the model circulation of Dinniman and Klinck (2004) compared favorably to that inferred from observations and the model intrusion occurs at a frequency close to that indicated by the mooring data (Moffat et al. 2009), baroclinic eddies at such high latitudes are barely resolved in these models

Corresponding author address: Yu Zhang, GFDL/Princeton University, 201 Forrestal Rd., Princeton, NJ 08540.
E-mail: yuz@princeton.edu

and it is difficult to relate the driving agents suggested by Dinniman and Klinck (2004) and Dinniman et al. (2011) to the small-eddy structures concurrent with the intrusion.

Here, we hypothesize that the ACC drives the cross-isobath transport through eddy–topography interactions. Both the eddy formation in the ACC and the encounter of eddies with the shelf are episodic, resulting in intermittent but persistent cross-isobath exchange. The hypothesis is made based on the following reasons: First, the ACC is an energetic, turbulent current where mesoscale eddies are ubiquitous. Because of the lack of meridional boundaries at latitudes of Drake Passage, mesoscale eddies are essential in the ACC dynamics. Second, the ACC is in close proximity to the shelf break in the WAP region (Orsi et al. 1995). Third, the Antarctic Slope Front, a density front usually found in continental margins of the Antarctic continent, is absent along the WAP (Jacobs 1991; Whitworth et al. 1998), which means the ACC can directly interact with the shelf.

Despite the lack of direct observational evidence over the WAP shelf, the eddy-driven cross-shelf transport has long been observed in other coastal areas. Its intermittent nature is typical for regions near strong, oceanic currents (Garfield and Evans 1987) but has not been addressed in prior theoretical studies. Instead, the interaction is commonly considered between a topography and a "single" eddy that is specified as the initial or boundary condition. Various interaction processes can be explored thoroughly by varying the eddy's strength, size, or initial location as well as the topography's profile, but the response to the intermittent forcing of an oceanic current cannot be inferred from the single-eddy–topography interaction in any simple way. What is also neglected in the prior literature is the effect of the shelf geometry, which was mostly assumed to be either infinite (Wang 1992; White and McDonald 2004) or bounded by a straight coast (Frolov et al. 2004). The effect of a straight coast is straightforward: it makes the eddy translate along the wall as required by the no-normal-flow condition, but a curved coast is more complex. Zhang (2009) and Zhang et al. (2011) considered the interaction between a topography and a single eddy in the presence of a shoreward-indented coast, enclosing the shelf into a bay and producing a variation of the shelf width. It was found that the propagation of topographic waves tends to be prevented in the narrow-shelf region, inducing the wave–coast interaction that produces strong cross-shelf transport. Because the topographic waves propagate along the topography only in one direction and have higher potential vorticity (PV) on the right, the wave–coast interaction as well as the intense cross-shelf transport only occurs near one side boundary of the bay but not the other.

We explore the ACC-driven cross-shelf transport and the shelf circulation in the WAP region using a two-layer primitive equation model with a reentrant, circumpolar channel adjacent to a continental slope and a bay-shaped shelf. The turbulent nature of the ocean current is most relevant to our study; other aspects such as the zonal transport or meridional overturning circulation are equally important for the ACC dynamics but are less crucial for the intermittent eddy–topography interaction. Therefore, only wind forcing is included, whereas thermodynamics are ignored. Furthermore, the continental slope is assumed to be zonally uniform. With these idealized configurations, the model ACC cannot be an accurate simulation to the real ACC, but it is able to spontaneously and continuously shed eddies that will drive the cross-slope/cross-shelf transport by interacting with topography. The intermittent eddy–topography interaction in the lower layer is found to induce the formation of an upper-layer PV front between the model ACC and the shelf. This newly formed jet in turn drives the water out of the bay and off the upper-ocean topography. Topographic waves are excited frequently over the slope, propagate westward along the isobath, and interact with the curved coast to enhance the cross-isobath transport near the western edge of the bay. A steady clockwise circulation results from ACC–shelf interactions, and the southeast region of the bay is suggested to be a retention area for passive tracers like Antarctic krill.

We describe the model configuration in section 2 and examine the formation of a second PV front in the upper ocean in section 3. The ACC-driven cross-isobath transport and shelf circulation are studied in section 4. Conclusions are given in section 5.

2. Model configuration

We use the Hallberg isopycnal model (HIM) (Hallberg and Rhines 1996), which solves the hydrostatic primitive equation in isopycnal coordinates and conserves the mass of each isopycnal layer in the absence of explicitly parameterized diapycnal mixing. The model ACC is assumed to be driven solely by a steady wind stress and flows eastward in a two-layer channel on a β plane in the Southern Hemisphere ($f < 0$). The continental slope in the WAP region is idealized as a zonally uniform slope lying against the southern boundary and extending into the upper ocean. In addition, the channel's southern boundary is bent shoreward (southward) to form a barotropic, flat-bottomed bay area that mimics Marguerite Bay. Features like rough topography, baroclinicity, and wind stress within Marguerite Bay are ignored for simplicity. The wind stress in the channel is also assumed to be time and zonally invariant. Results of three
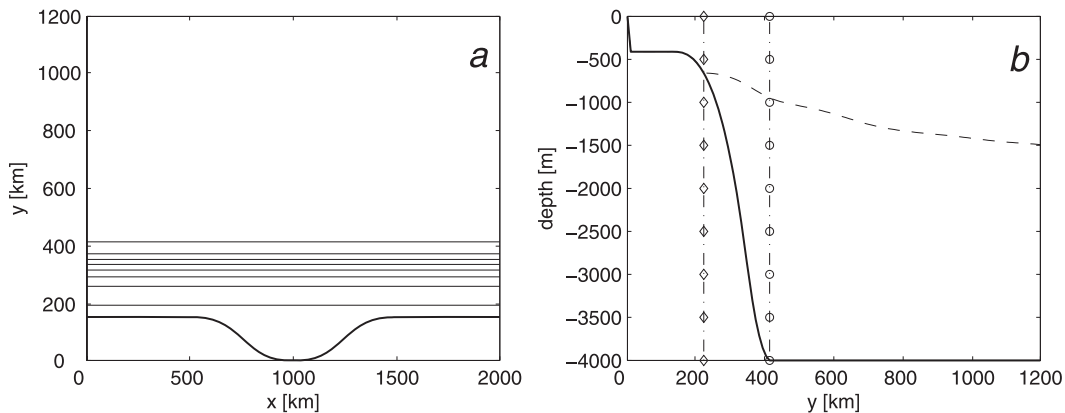
FIG. 1. (left) Top view of the model domain for case BAY. The thick solid line denotes the southern boundary of the channel, and the thin solid lines are depth contours with intervals of 400 m. (right) Side view of the topography (thick solid line) and the layer interface (dashed line) in the quasi-equilibrium state in case BAY. The line with diamonds denotes the edge of the first-layer slope, and the line with circles denotes the base of the topography.

eddy-resolving simulations with a uniform horizontal resolution of 10 km are presented. The model domain extends 2000 km in the zonal direction and has a straight northern boundary at $y = 1200$ km. Only in the third simulation, case BAY, both a high continental slope and a bay are present (Fig. 1b). The bay area is enclosed between the indented southern boundary and the latitude of $y = 155$ km, starting from where the water depth increases northward over the slope until $y = 400$ km (Fig. 1a). The wind stress applied to the first layer has a sinusoidal profile,

$$\tau = \begin{cases} \tau_0 \sin\left[\dfrac{\pi(y - Y_s)}{L_c}\right] & \text{if} \quad y >= Y_s \\ 0 & \text{otherwise,} \end{cases} \quad (1)$$

where $\tau_0 = 0.12$ N m^{-2} sets the wind stress amplitude, $Y_s = 155$ km guarantees zero wind stress within the bay, and L_c denotes the meridional range of the nonzero wind stress.

The other two simulations also depict the channel flow but have no bay area; that is, both the channel's northern and southern boundaries are aligned with latitudes. The first experiment, case FB, simulates the flow in a flat-bottomed channel and is readily compared to the flat-bottomed simulation in QG models (McWilliams et al. 1978). The second simulation, case SB, has the intermediate complexity among the three and is designed to investigate the role of the topography in dynamics of the model ACC. It differs from case FB only at its sloping bottom: a small, linear, continental slope is constructed within 200 km of the southern boundary and is entirely submerged in the lower layer (Fig. 6a). The wind stress profile in both cases is still sinusoidal as described in Eq. (1) but is symmetric about the central latitude with

$Y_s = 0$ and $L_c = 1200$ km. The wind stress amplitude $\tau_0 = 0.15$ N m^{-2} in cases FB and SB is larger than that in case BAY. This is because stronger wind stress along with high topography in case BAY may cause the interface to rise above the topography, bringing lower-layer water onto the shelf. This situation is potentially relevant to the onshore intrusion of the Lower Circumpolar Deep Water (LCDW) (Moffat et al. 2009) but is out of the scope of the current study. On the other hand, varying the wind stress amplitude in cases FB and SB does not cause qualitative differences of the model results.

To balance the eastward momentum input of the surface wind, the horizontal momentum is dissipated in the second layer by a quadratic drag with a coefficient $C_d = 0.001$. The model ocean spans 4000 m in depth, having the first layer occupy the upper 1000 m in cases FB and SB and 1200 m in case BAY when the ocean is at rest. With the reduced gravity $g' = 0.02$ m s^{-2} and the Coriolis parameter $f_0 = -1.1 \times 10^{-4}$ s^{-1}, the internal deformation radius is around 35 km. This scale is much greater than the first deformation radius in the WAP region but ensures that mesoscale eddies can be well resolved in the model. Unresolved, subgrid-scale motions are dissipated horizontally through a biharmonic friction with a viscosity $A = 1.5 \times 10^9$ m^4 s^{-1}; free-slip boundary conditions are applied at side boundaries preventing momentum flux through solid walls.

In all three simulations, the model ocean starts from rest. A small perturbation is added in the center of the channel after the flow becomes unstable, triggering the development of a vigorous eddy field and a transient period of about several thousand days (Fig. 2). The flow finally reaches a quasi-equilibrium state in which the layer energy varies around a mean state with a small amplitude but without any noticeable trend. All simulations are
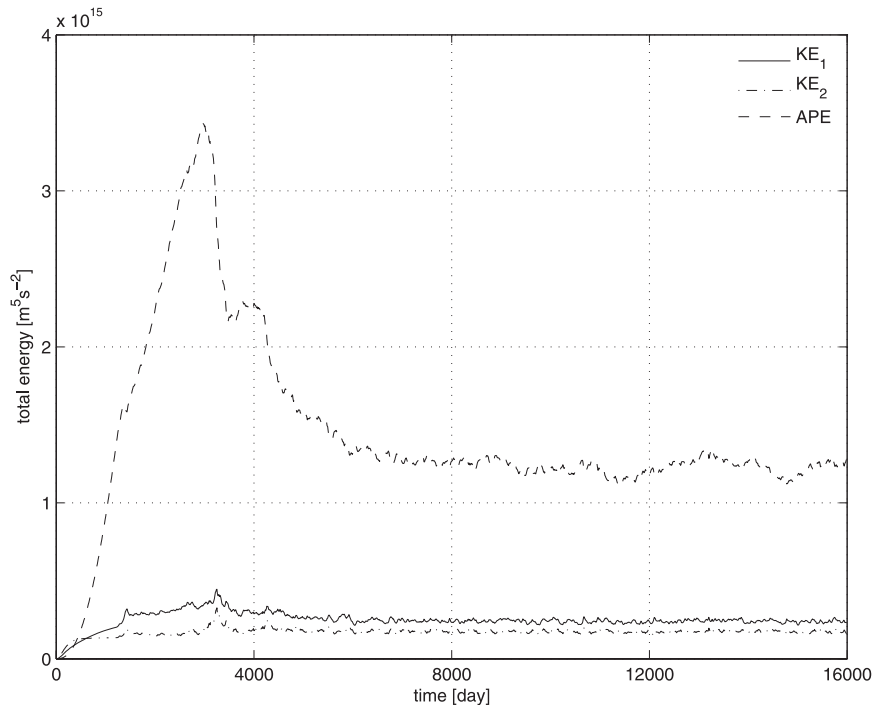
FIG. 2. Time evolution of the total kinetic energy in the first layer (solid line), the second layer (dash–dot line), and potential energy associated with the layer interface (dashed line) in case BAY.

run for at least 10^4 days and the mean quantities are referred to results averaged both in x and in time over the final 4000 days.

It is noted that idealized configuration of the model topography affects the direct comparison of the model results to the real ocean, as does the absence of the diabatic processes. In the widely accepted theory of the ACC dynamics proposed by Munk and Palmén (1951), the bottom form drag, a force associated with the pressure difference between the upstream and the downstream sides of submarine ridges or seamounts, is essential in providing the necessary sink of the eastward momentum. It was also suggested that the zonal transport and eddy kinetic energy (EKE) are greatly reduced in the presence of the form drag (McWilliams et al. 1978). In our model simulations, the ocean bottom is either flat or zonally uniform, causing the absence of the form drag and hence excessive volume transport as well as EKE compared with observations.

3. Formation of a second jet over the lower-layer topography

The flow of the ACC is well known to be concentrated in several jets associated with density fronts (Orsi et al. 1995; Belkin and Gordon 1996), and the three most distinguishable circumpolar fronts are the Subantarctic Front, the Polar Front, and the Southern ACC Front, which each extend into the deep ocean. The Southern ACC Front is right along the outer WAP shelf break (Orsi et al. 1995), suggesting the direct influence of the ACC. As a robust feature of observations, the multiple-jet structure was also indicated by the eddy-resolving numerical models of the Southern Ocean (Lee and Coward 2003; Hallberg and Gnanadesikan 2006), but the dynamics regarding the jet formation is still largely obscure. In most literature, the formation is attributed to the theory put forward by Rhines (1975) in which the meridional gradient of the planetary vorticity (the β effect) was found to arrest the inverse cascade of the decaying barotropic turbulence and organize the flow into zonal jets. The corresponding meridional scale of the jets is given by $k = (\beta/2U_e)^{1/2}$, where k is the meridional wavenumber and U_e is the characteristic eddy velocity. The bottom topography sloping in the meridional direction was found to be able to influence the formation of the jets in numerical models (Sinha and Richards 1999; Thompson 2010). The slope was conjectured to provide an analogy of the β effect, augmenting or reducing the restoring forcing of the planetary vorticity gradient as well as the "effective" Rhines scale (Sinha and Richards 1999). More recently, a new mechanism of the jet formation was proposed by Berloff et al. (2009). They explained the dynamics of jets in terms of the linear stability
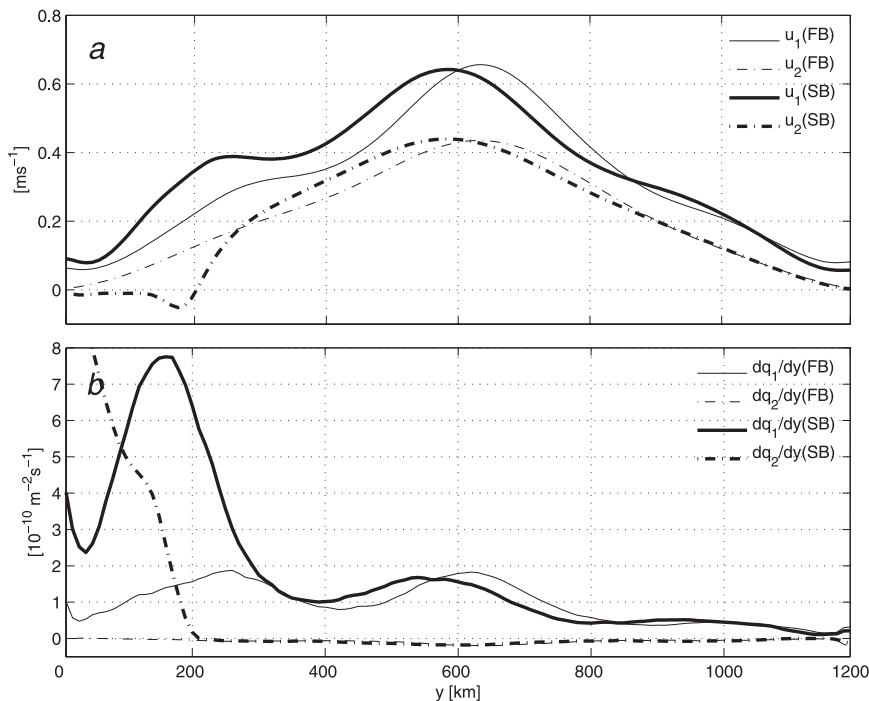
FIG. 3. (top) Time-mean along-slope velocity plotted against the cross-slope distance in the first layer (solid lines) and the second layer (dash–dotted lines) in case FB (thin lines) and case SB (thick lines). (bottom) Time-mean meridional gradient of potential vorticity in the first layer (solid lines) and in the second layer (dashed–dotted lines) in case FB (thin lines) and case SB (thick lines).

of the background flow and the self-interactions of the linear eigenmodes and suggested that there is no simple and universal scaling for the meridional jet scale.

It is shown in the following that including a zonally oriented bottom slope in a zonal channel causes the formation of a jet and that the formation mechanism is closely related to the eddy–topography interactions.

a. Flat-bottomed simulation

We start with the simulation, case FB, in a flat-bottomed two-layer channel with two straight boundaries along latitudes of $y = 0$ and $y = 1200$ km. The steady zonal wind has a half-sine profile with the maximum at $y = 600$ km and the initial first-layer thickness is uniformly 1000 m. Our model results are very similar, both qualitatively and quantitatively, to those of the flat-bottomed QG simulation in McWilliams et al. (1978).

The mean (time and zonally averaged) zonal velocity profiles show a jet centered around the middle latitude in both layers (Fig. 3a). The maximum value of the upper-layer jet is over 0.6 m s^{-1}, whereas that for the lower-layer jet is about 0.4 m s^{-1}. The EKE also weakens from the jet axis as well as from the first layer with its maximum value of over 800 cm^2 s^{-2} at the surface (Fig. 4a).

Both the maximum zonal velocity and EKE are at least 2 times larger than those from the direct current measurements in the energetic Subantarctic Front south of Australia (Phillips and Rintoul 2000). Furthermore, the total transport carried by the model ACC is about 1140 Sv (1 Sv $\equiv 10^6$ m^3 s^{-1}), excessively greater than what is observed. These differences from the real ocean are consequences of idealized configurations such as the zonally uniform slope.

Although similar in some aspects to the flat-bottomed QG simulation, the model results also demonstrate a striking difference: the flow, especially the upper-layer flow, is not symmetric about the jet axis. A "plateau" appears on the first-layer velocity profile between $y = 200$ km and $y = 400$ km, different from that in the symmetric region about the jet axis. Meanwhile, a second local maximum of the PV gradient is found near the region of the velocity plateau with the amplitude even slightly larger than that at the jet axis. It will be shown that this axis asymmetry is related to the big variation of the layer thickness allowed in the primitive equation model.

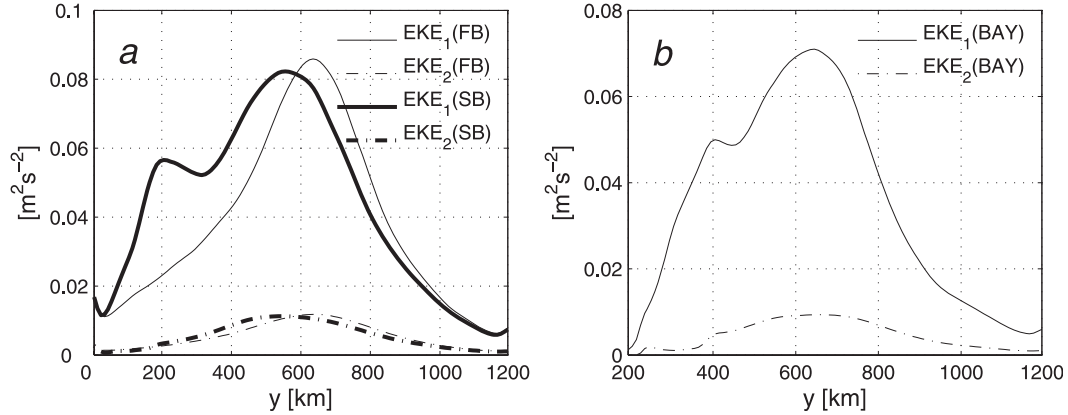We begin with the equation for the mean zonal momentum and the layer thickness,

FIG. 4. (left) EKE in the first layer (solid lines) and the second layer (dashed–dotted lines) in case FB (thin lines) and case SB (thick lines). (right) EKE in the first layer (solid line) and second layer (dashed–dotted line) in case BAY.

$$\frac{\partial}{\partial t}\overline{u}_i - \overline{q_i \cdot v_i h_i} = \overline{D}_i + \overline{F}_i \quad \text{and} \tag{2}$$

$$\frac{\partial}{\partial t}\overline{h}_i + \frac{\partial}{\partial y}\overline{h_i v_i} = 0, \tag{3}$$

where bars denote the mean quantities, q_i denotes the layer PV, $(f + \zeta_i)/h_i$, D_i represents the lateral friction, and F_i denotes the surface wind stress $\tau/\rho h_1$ in the first

layer and the bottom drag $-(C_d/h_2)|u_2|u_2$ in the lower layer. Following Plumb and Ferrari (2005), we define the residual circulation as

$$\overline{v}_i^* \equiv \frac{1}{H_i}\overline{v_i h_i}, \tag{4}$$

where H_i is the volume-averaged layer thickness. Substituting (4) into (2) and (3) gives
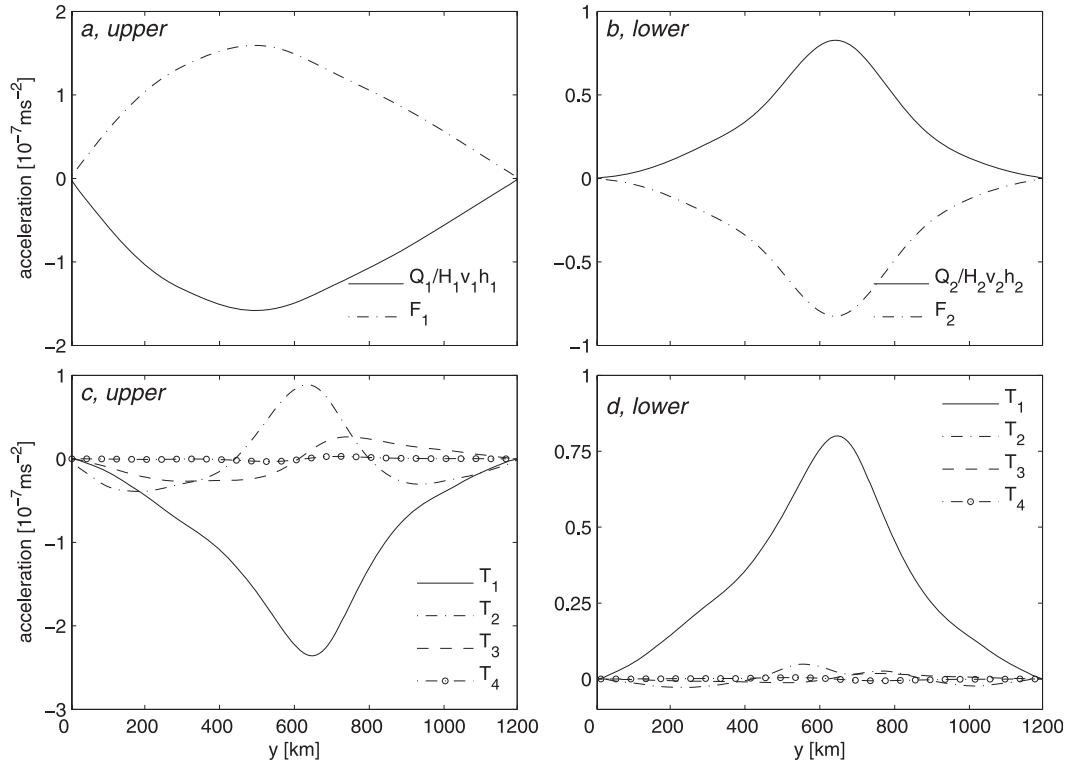

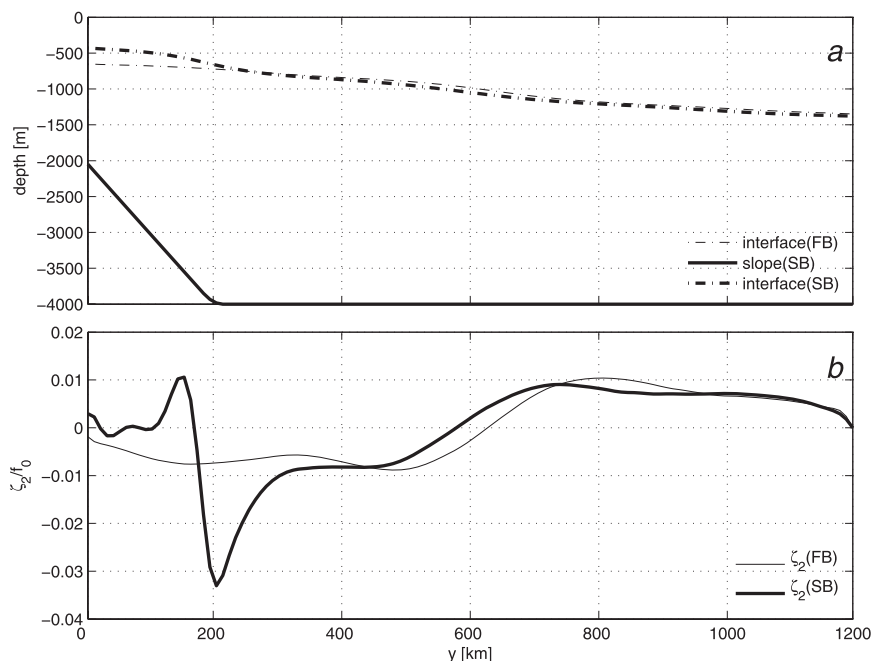FIG. 5. Various terms in the zonal momentum equation [Eq. (7)] for case FB.

FIG. 6. (top) The mean interface in case FB (thin dashed–dotted line) and in case SB (thick dashed–dotted line) with the thick solid line depicting the bottom slope in case SB. (bottom) The mean relative vorticity in case FB (thin solid line) and case SB (thick solid line).

$$\frac{\partial}{\partial t}\overline{u}_i - f_0\overline{v}_i^* = \overline{\frac{Q_i}{H_i}v_i h_i} + \overline{D}_i + \overline{F}_i \quad \text{and} \quad (5)$$

$$\frac{\partial}{\partial t}\overline{h}_i + H_i\frac{\partial}{\partial y}\overline{v}_i^* = 0, \quad (6)$$

where $Q_i/H_i \equiv \{[(f + \zeta_i)/h_i] - (f_0/H_i)\}$ represents the PV anomaly from the background value (f_0/H_i) At the quasi-equilibrium state, the time tendency terms $\partial/\partial t$ are small and negligible and the normal velocity at solid walls has to vanish, so Eq. (6) gives $\overline{v}_i^* = 0$ at all latitudes. The momentum balance, as indicated by (5), is closed between the PV flux $(Q_i/H_i)v_i h_i$ and the external forcing $\overline{F}_i$ (Figs. 5a,b). In the upper layer, the PV flux acts as a sink of the eastward momentum, balancing the surface wind, whereas, in the lower layer, it drives the eastward flow and provides the momentum that is to be dissipated by the bottom friction. The PV flux is dominated by the eddy transfer, which is clearly demonstrated if we decompose it into four components,

$$\overline{\frac{Q_i}{H_i}v_i h_i} = -\frac{f_0}{H_i}\overline{v_i' h_i'} + \overline{v_i'\zeta_i'} + \left(f\overline{v}_i - \frac{f_0}{H_i}\overline{v}_i\overline{h}_i\right) + \overline{\zeta}_i\overline{v}_i,$$
$$= T_1 + T_2 + T_3 + T_4, \quad (7)$$

where primes denote perturbations from the mean. The first two terms, T_1 and T_2, are induced by eddy motions and represent the interfacial form drag (Vallis 2006) and

the horizontal Reynolds stress divergence, respectively; term T_3 is related to the mean flow, and T_4, which is a mean flow vortex term, is quite small and negligible (Figs. 5c,d). In both layers, the Reynolds stress divergence T_2 concentrates the jet in the central latitudes and decelerates the flow in flanks, implying that the baroclinic instability is the major mechanism tapping the available potential energy from the mean to feed the growth of eddies. The interfacial form drag T_1, however, works differently in the two layers: it acts to retard the flow in the upper layer while driving the flow in the deeper ocean with similar but opposite amplitudes. It differs from the Reynolds stress divergence, which redistributes the momentum horizontally without producing any net momentum loss or gain for each layer. The interfacial form drag actually transfers momentum downward and is therefore essential for the lower-layer fluid that is shielded from the direct wind forcing.

The term T_3 is very small in the lower layer but is of the same order as the Reynolds stress divergence in the upper ocean. Moreover, the way it influences the mean flow is different from both eddy-induced forces, which are roughly symmetric about the jet axis. It is antisymmetric about the jet core, strengthening the flow in the northern half of the domain but weakening the flow in the southern half. The big amplitude of the term T_3 in the upper ocean results from the large meridional variation of the layer thickness, which is as large as 700 m
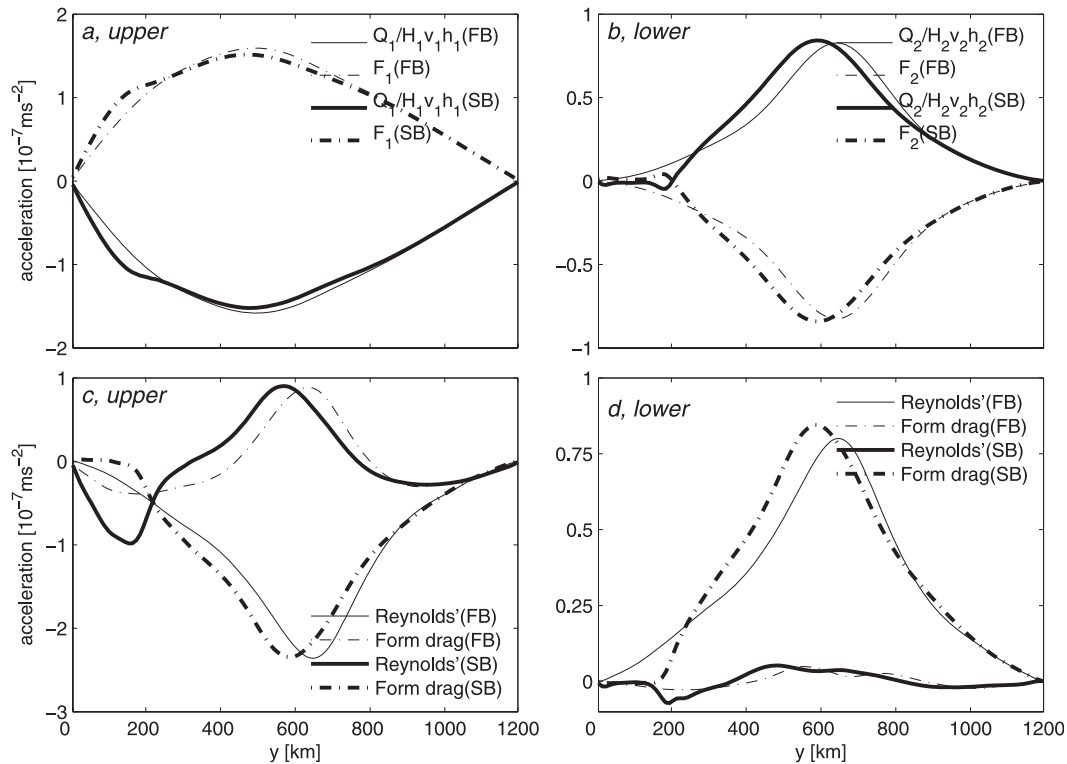
FIG. 7. Various terms in the zonal momentum equation in case FB (thin lines) and case SB (thick lines).

(Fig. 6a). The variation of such a large amplitude in layer thickness is not allowed in QG models, and we believe it is the reason for the asymmetric shape of our model flow, which represents the major difference from McWilliams et al. (1978).

b. Sloping-bottomed simulation

The second simulation, case SB, is carried out in the same zonal channel with the same configuration as in case FB, except that a zonally uniform, linear slope is constructed within 200 km of the southern boundary, introducing the northward increase of the water depth from 2000 to 4000 m (Fig. 6a). The addition of the bottom slope to the model does not change the turbulent feature of the flow. Results of case SB are quite similar to those of case FB over the flat bottom (to the north of $y = 200$ km), but, near the base of the slope, new features arise as an additional jet and an upper-layer PV front. The jet is eastward in the upper ocean but reverses sign in the lower layer. The new, upper-layer PV front is identified as a local maximum of the PV gradient with the amplitude much greater than that at the jet axis (thick line in Fig. 3). The rapid increase of the PV gradient from the interior toward the slope is to a large extent caused by the southward increase of the steepness of the layer interface, $-(f/h_1^2)(\partial h_1/\partial y)$. As the ocean

depth increases northward over the topography, the sign of the PV gradient in the lower layer is positive above the slope, opposite to that off the slope but the same as that in the first layer (Fig. 3b). The necessary condition for baroclinic instability is therefore not satisfied in the sloping region, suggesting a stabilizing effect of topography. This is consistent with Sutyrin et al. (2001) and Wang and Ikeda (1997), in which eddies in the deep ocean were found to be important in the eddy pinch-off process of the meander above them but have their effects suppressed in the presence of a positive bottom slope (same sense as isopycnal tilt as in the current simulation).

The formation of the second PV front over the sloping bottom can be explained by eddy–topography interactions. Because lower-layer eddies interact with the slope, they force water exchange between the sloping region, where the ambient PV is negative and large, and the flat-bottomed region, where the ambient PV is only weakly negative. Water columns pushed onto the slope are squeezed, and, to conserve PV, they generate positive relative vorticity with counterclockwise circulation as well as higher interface. Conversely, water columns dragged down the slope are stretched and form negative relative vorticity with clockwise circulation and suppressed interface. On the meridional profile of the mean lower-layer relative vorticity (Fig. 6b), there exists a narrow
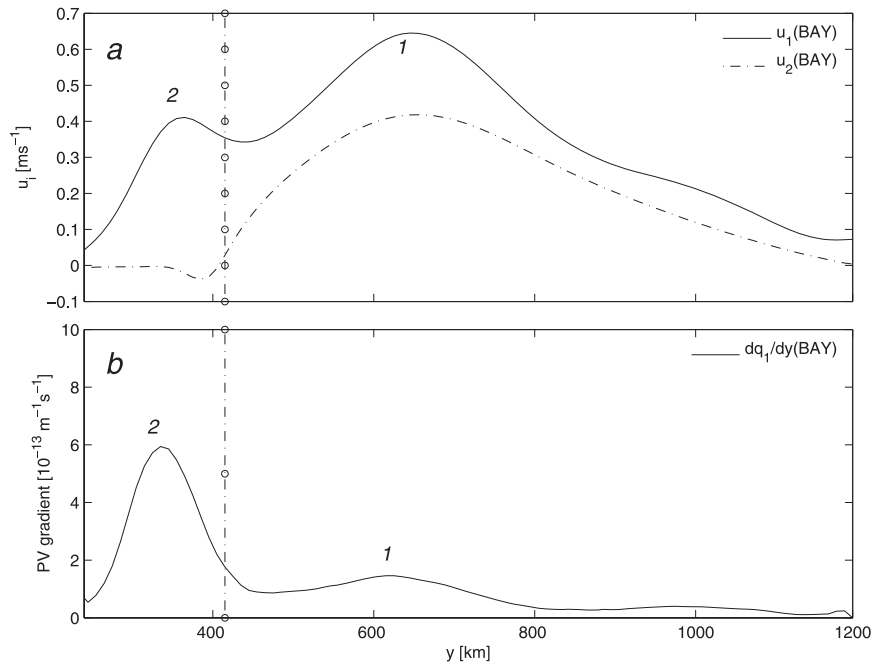
FIG. 8. (top) Mean zonal velocity in case BAY in the first layer (solid line) and the second layer (dashed–dotted line). (bottom) Mean PV gradient in the upper layer in case BAY. The dash–dot–circle lines denote the base of the topography. Here, 1 denotes the main jet/PV front near the center of the channel and 2 denotes the jet/PV front induced by the eddy–topography interaction in the lower layer.

band of positive relative vorticity right next to the slope edge in the south and a wider band of negative vorticity in the north, which both have amplitudes much greater than those without topography. The small meridional width of the band of the positive relative vorticity compared with the width of the slope is reminiscent of the "effective range" of the anticyclone–slope interaction in Zhang (2009). In the presence of a smooth slope topography, the effect of the baroclinic forcing anticyclone is limited by its small decay length scale and counteracted by the topographic waves (Zhang 2009). The influence of the anticyclone cannot reach far onto the slope, and the effective range is on the order of the deformation radius. Furthermore, the layer interface in the sloping-bottomed simulation is further raised toward the south in the same way as the ocean bottom (Fig. 5a), contributing to the strengthening of the PV gradient in the first layer through the term $-(f/h_1^2)(\partial h_1/\partial y)$. Both of these features, the bands of the positive and negative relative vorticity and the rise of the interface, suggest the common occurrence of the eddy topography interaction along the slope, which, as explained in the following, causes the formation of a second front.

A direct consequence of the exchange across the slope edge is a negative meridional PV flux over the slope,

opposite to the flux in the rest of the lower layer (Fig. 7b). The negative PV flux is concentrated within a very small region near the slope edge, whereas it is nearly zero farther onto the slope. This is again a manifestation of the small effective range of the eddy–topography interactions. Because the PV flux is the only driving force in the lower ocean balancing the bottom drag and it provides westward instead of eastward momentum in that small region near the slope edge, the jet corresponding to this negative PV flux is directed westward. The two major components of the PV flux, the Reynolds stress divergence, and the interfacial form drag adjust themselves to fit into the PV flux profile. The interfacial form drag declines quickly southward from the jet axis to nearly zero at the slope edge, and the Reynolds stress divergence has its amplitude decreased from the slightly negative value in the flat-bottomed case (Fig. 7d). An important feature of the interfacial form drag is that the force on each layer due to the other is equal and opposite. In response to the rapid decline in the second layer, the first-layer interfacial form drag, which has negative value in case FB, increases rapidly toward zero approaching the slope edge. On the other hand, the momentum input by the wind remains largely the same in the two cases, so, with diminishing interfacial form drag over the slope, the Reynolds stress divergence has its amplitude greatly enhanced (the
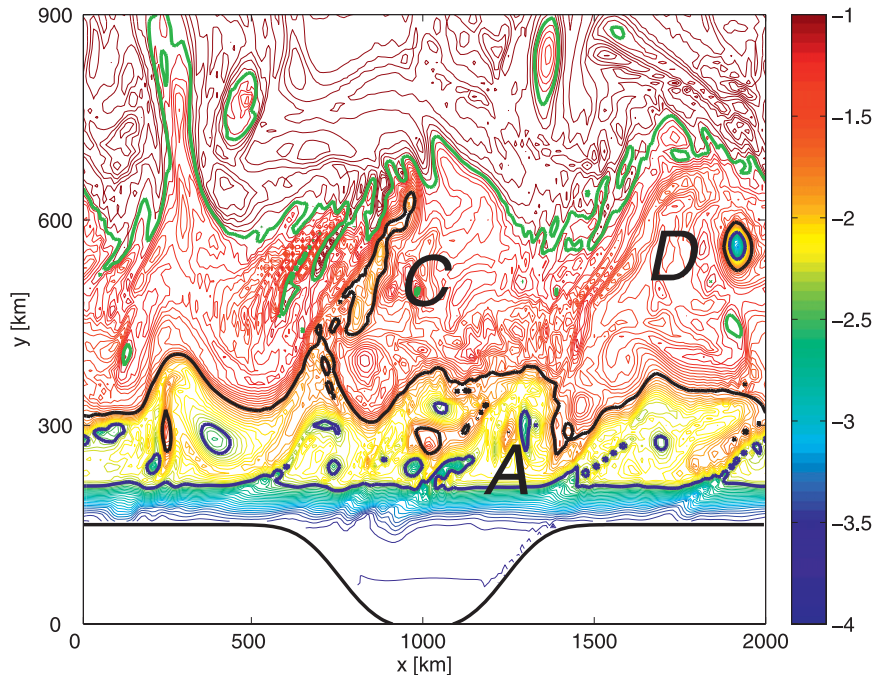
FIG. 9. A snapshot of first-layer PV normalized by $|f_0|/1200$ m. The thick green line denotes the main jet; the thick black line denotes the second PV front; and the thick blue line denotes the PV contour along the first-layer slope edge.

value is further decreased because it is negative) to balance the wind stress. As noted before, the layer integral of the Reynolds stress has to be zero; therefore, a more global adjustment occurs, increasing the Reynolds stress divergence between the main jet axis and the latitude of the slope edge. The combined effect of the decrease over the sloping bottom and increase over the flat region of the Reynolds stress divergence causes the formation of a second eastward jet in the first layer.

Overall, the eddy–topography interaction in the lower layer changes the local structure of the meridional PV flux. Through the interfacial form drag, the first layer ''feels'' the existence of the topography and makes an adjustment of the horizontal momentum flux, which further changes the characteristics of the mean flow in the first layer. Meanwhile, the interface is further raised toward the south because of the lower-layer eddy–topography interactions. Modifications in the layer thickness and the mean flow structure contribute to the enhancement of the PV gradient over the slope in the upper ocean. Along with the formation of the second PV front and jet, the upper-layer EKE is also strengthened in the same region (thick line in Fig. 4a), suggesting the local intensification of the eddy activity.

One may wonder whether the front-like structure represented by the second maximum of the PV gradient and the plateau of the velocity observed in case FB is

a precursor and imperative for the second PV front observed in case SB. The answer is no. The two fronts have different formation mechanisms: the one in case FB is related to the big layer-thickness variation, whereas the one in case SB is the consequence of adding a bottom slope.

A related question is whether the slope direction is critical for the formation of the second PV front: that is, what if the same bottom slope is constructed against the northern boundary rather than the southern one? Then the topographic slope is negative in the sense that it is opposite to the large-scale slope of the interface, which falls toward north as forced by the wind stress. This situation resembles that of the Labrador Current, whereas the setting in our simulation is similar to that of the Gulf Stream. Whether the eddy interaction with a negative slope can still induce the formation of an upper-ocean PV front over topography is an interesting problem but is not our concern in the present paper.

c. Simulation with a bay

In the third simulation, case BAY, a much wider as well as higher slope is added to the bottom, extending all the way into the first layer and intersecting the interface around $y = 220$ km at the equilibrium state. The entire bottom slope is therefore separated into two parts: the second-layer slope below the interface and the first-layer
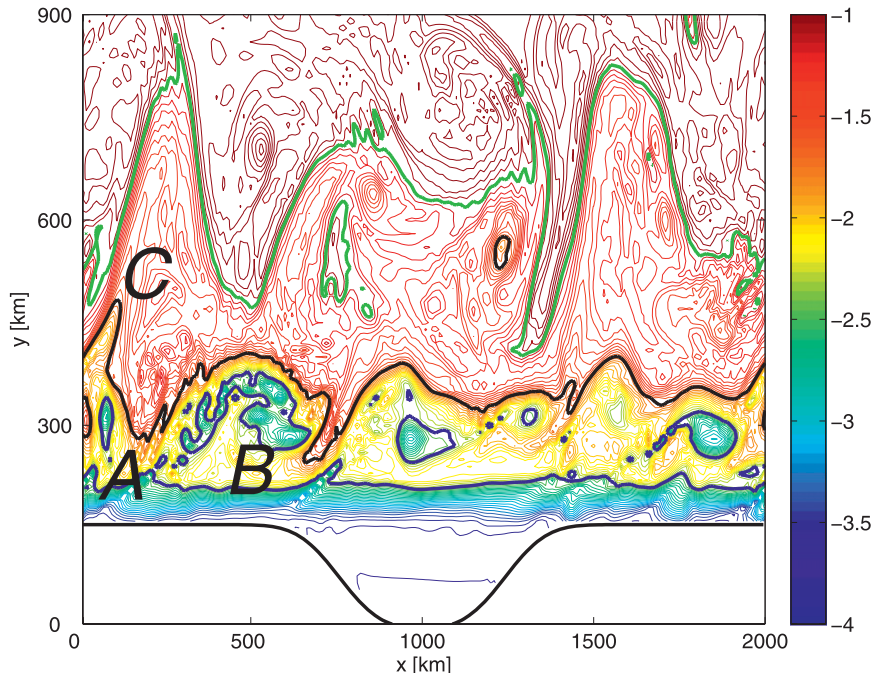
FIG. 10. As in Fig. 8, but for at a different time.

slope above. The latter is about 70 km wide and is connected at $y = 155$ km with a flat-bottomed shelf, which is enclosed by the curved coast (Fig. 1). Although the bottom topography and the model domain are different from case SB, a second zonal jet and a second upper-layer PV front still form out of the eddy interaction with the lower-layer topography (denoted as 2 in Fig. 8). The associated maximum velocity and the maximum PV gradient occur between the base of the slope around $y = 400$ km and the intersection latitude, with amplitudes comparable or even larger than those at the jet axis (denoted as 1 in Fig. 8).

Figures 9 and 10 show two snapshots (300 days apart) of the first-layer PV in case BAY, in which the PV front near the center of the channel is denoted by a thick green line, the second PV front resulting from lower-layer eddy–topography interaction is denoted by a thick black line, and the water over the first-layer slope is in blue with its northern edge marked by a thick blue line. Sandwiched between the first-layer slope and the main jet in a relatively narrow region, the second PV front shields the first-layer slope from direct influence of the main jet but is meanwhile perturbed by the main jet and forces the slope water with its own variability. There are three kinds of interaction processes involved. First, the second PV front interacts with the first-layer slope with its shoreward meander or with anticyclones pinched off from the front. The counterclockwise circulation associated with both structures drives the slope water off the topography into the open ocean in forms of isolated

cyclones (A in Fig. 9) or streamers (A in Fig. 10). Second, the slope water that has been driven off the topography may further interact with a meander of the second PV front with its clockwise circulation, amplifying the amplitude of the meander or making the meander close upon itself into an isolated anticyclone (see B in Fig. 10). Sometimes, through interaction with the second PV front, the topographic eddy may manage to cross the front into the interior (see D in Fig. 9). Third, the seaward meander of the second PV front interacts with the shoreward meander of the main jet that is near the center of the channel (see C in Figs. 9, 10), inducing pinch off of eddies from both fronts. The first kind of interaction directly contributes to the cross-slope/cross-shelf transport and shelf circulation and is the main focus of the next section.

4. Cross-slope/cross-shelf transport and shelf circulation

We use passive tracers that are advected by the model flow without any explicit diffusivity to investigate the cross-slope/cross-shelf exchange and shelf circulation driven by the open-ocean jet. One way to specify the tracer distribution is to fix its concentration in time. For example, if the tracer concentration is fixed at 1 to the south of some specific latitude and 0 to the north of it, then the volume flux of the tracer across that latitude indicates the rate at which the water is exchanged
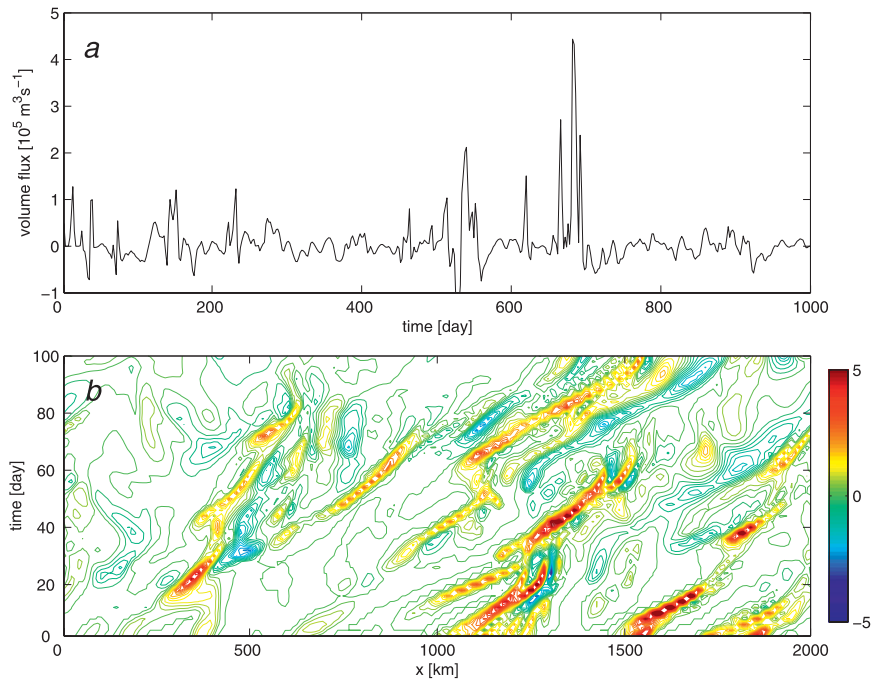
FIG. 11. (top) Time series of the volume flux of tracer A; whose concentration is initially 1 to the south of the latitude at $x = 1000$ km, $y = 220$ km during a subperiod. (bottom) The x–t plot of the tracer A flux in the same subperiod.

between the two regions. Alternatively, we could specify the initial tracer concentration as 1 and 0 across some latitudes, respectively, and let the concentration evolve in time as tracers are carried around by water particles. Compared with the first approach, the second method can show us the evolution of the tracer front, which is a vivid demonstration of the Lagrangian rather than Eulerian circulation over topography and is therefore adopted in the present study. One limitation of this method is that, as time goes on, more and more tracer is advected across its 1–0 boundary, the interface between 1 and 0 in initial distribution, into the deeper ocean, so the concentration in the shallow region declines and the instantaneous volume flux of the tracer across the 1–0 boundary drops. Then the long-term mean volume flux would be an underestimate of the mean exchange rate. To overcome this limitation, we average the volume flux through a relatively short period of time during which the variation of the tracer concentration is not noticeable. We carried out 10 consecutive simulations, which are each 1000 days long and have the tracer concentration reinitialized at the beginning; typical results of all these simulations are discussed in the following.

In the interaction between a barotropic eddy and a step topography (Zhang 2009; Zhang et al. 2011), two mechanisms were found to govern the cross-isobath transport, the advection by the forcing eddy and the propagation of topographic waves. Topographic waves are similar to the planetary Rossby waves in that, in the absence of other factors such as the mean flow, they propagate along the isobath in only one direction, having higher PV on the right. In addition, because the restoring forcing of the topographic waves is provided by the variation of the ocean bottom, they have amplitudes that decay away from the topography. The two mechanisms tend to advect the PV front deformations in opposite directions in the anticyclone-induced interactions, generating the cross-shelf transport in the form of an isolated topographic cyclone moving with the forcing anticyclone into the deep ocean. In the baroclinic interaction of a single eddy with a smooth slope, the decay length scale of the forcing eddy is on the order of the internal deformation radius; the strength of the eddy advection was seen to decline quickly shoreward, whereas the wave propagation becomes increasingly significant for the cross-isobath transport (Zhang 2009).

In the current model, the two control mechanisms are found to dominate the cross-isobath transport near the open ocean and near the coast, respectively. We define the exchange across the mean intersection line of the slope with the layer interface or the first-layer slope edge as the cross-slope exchange and that across the flat-bottomed shelf (also the bay) as the cross-shelf exchange. Tracer A
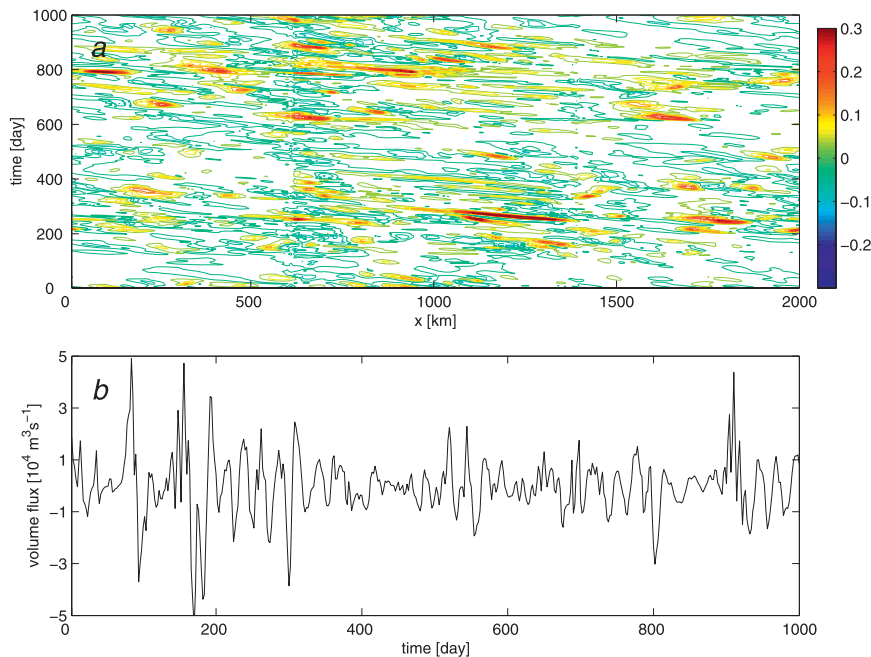
FIG. 12. (top) The *x–t* plot of the PV anomaly (total minus the time mean) normalized by $|f_0|/1200$ m along $y = 165$ km in case BAY. (bottom) Time series of the volume flux of tracer B, whose concentration is initially 1 inside the bay, at $x = 1000$ km, $y = 155$ km during a subperiod.

with 1–0 boundary along $y = 220$ km is adopted for the former process, and tracers such as tracer B, which has 1–0 boundary at the opening of or inside the bay, are used for the second process.

a. Cross-slope exchange

Near the slope edge, meanders or eddies of the second PV front induce strong advection to pull the slope water unidirectionally northward down the slope in the form of topographic streamers or cyclones. For a fixed location along the slope edge, the approach of anticyclonic eddies or meanders is intermittent. The time series of the cross-slope flux of tracer A is made up of a few large-amplitude pulse-like events separated by big intervals of quiet periods (Fig. 11a). Each event resembles the interaction between the topography and a single mesoscale, baroclinic eddy (Zhang 2009). The strong flux of each event, recognized as a bright patch in the *x–t* plot (Fig. 11b) is concentrated within a narrow region in *x* and is meanwhile deflected eastward because of the eastward advection of the forcing eddy or meander by the mean flow. We quantitatively define an event as the area in the *x–t* plot bounded by a contour along which the tracer flux drops to e^{-1} of its maximum value. From a single 1000-day simulation, 20 interactions with the strongest fluxes are located, and they carry about 35% of the total tracer transport. More strong-flux events occur

during the early intervals of the period: 16 out of 20 take place in the first 300 days and carry 28% of the total transport. This is because, as tracer mass is transported offshore by eddies, the tracer concentration quickly declines over the slope. No particular along-slope location is found favorable to the strong-flux events, indicating that the eddy–topography interaction or the impingement of the offshore variability onto the topography is generally homogeneous along the slope on time scales longer than 100 days. The time duration of these events is on the order of 10 days and is mostly between 10 and 20 days.

The time-mean volume flux of the slope water across the slope edge is underestimated if we average the tracer flux over the entire 1000-day simulation because, as noted above, the tracer concentration over the slope drops in time. Instead, we average the tracer flux over the first 100 days of each simulation and take the average over all simulations. The result shows a mean northward slope-water flux of 1.6 m^2 s^{-1} across the latitude of $y = 220$ km, implying an equal and opposite southward flux of deep-ocean water onto the slope. The northward slope-water flux is stronger than the Ekman flux under the strongest wind near the center of the channel, which is about 1.1 m^2 s^{-1} and directed northward. The wind stress amplitude used in our model is similar to those in a number of theoretical and modeling studies (McWilliams et al. 1978; Karsten et al. 2002). Also, the zonally integrated
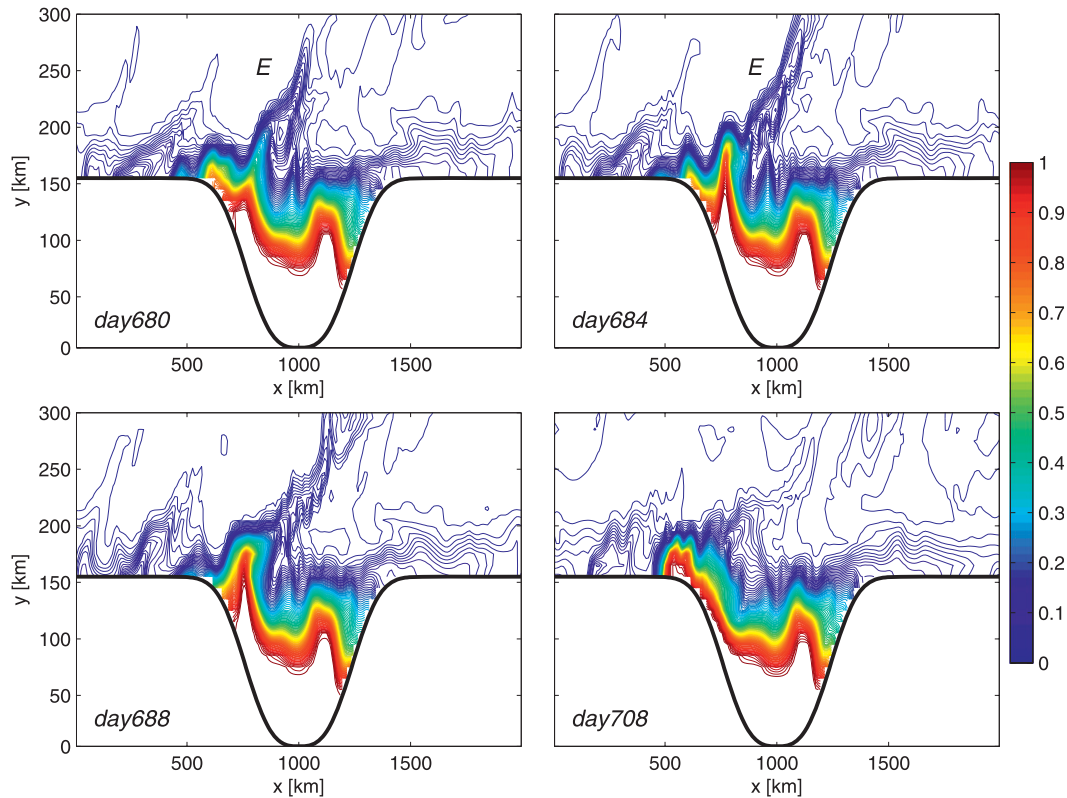
FIG. 13. Snapshots of the distribution of tracer B concentration.

Ekman transport is very close to that across a streamline near 60°S estimated from wind stress data of the Southampton Oceanography Center (Josey et al. 1998; Karsten and Marshall 2002). The ACC-driven cross-slope flux in the real ocean is probably smaller but still comparable to the Ekman flux given the fact that our model EKE has the maximum of about 700 cm^2 s^{-2} (Fig. 4b), much greater than observations in the ACC.

b. Cross-shelf transport

In the absence of surface wind stress, the flat-bottomed bay area is only forced by the time-dependent motion at its opening, which is about two deformation radii shoreward of the first-layer slope edge. As the direct advection by the deep-ocean variability drops quickly from the slope edge the velocity amplitude associated with the topographic waves becomes significant near the bay opening. These waves propagate westward along the slope in the Southern Hemisphere with shallow water in the south. Figure 12a shows the x–t plot of the PV anomaly at $y = 165$ km, a little bit seaward from the bay opening. In the figure, the anomalies clearly show a westward translation, which is against the eastward motion of the mean flow and is consistent with the propagation direction of the topographic waves. Because of the waves, the water particles

have a tendency to oscillate around their mean locations and the tracer previously carried away may be returned at a later time. The meridional flux of tracer B at a location along its 1–0 boundary, $y = 155$ km, oscillates around 0 in time, with positive and negative values of similar amplitudes (Fig. 12b). The cross-shelf transport, therefore, in no way can be explained by a linear summation of strong but independent flux events as the cross-slope transport is. It is by the cumulative effects of multiple waves excited by different offshore eddies that a water particle can be finally carried off the slope into the deep ocean. Nevertheless, the mean flux out of the bay, estimated in the same way as the flux of tracer A, is about 0.4 m^2 s^{-1} and also comparable with the Ekman flux in the channel.

Tracer particles over the flat-bottomed area are carried out of the bay and/or down the slope in two ways as found in all 1000-day simulations. First, as they move northward by the topographic waves, the advection by the offshore variability becomes increasingly strong, driving the particles down the slope along a northeastward route and in the form of streamers or topographic cyclones. A necessary condition for this process to be effective is that the tracer particles, disregarding their zonal locations, are close to the bay opening and hence
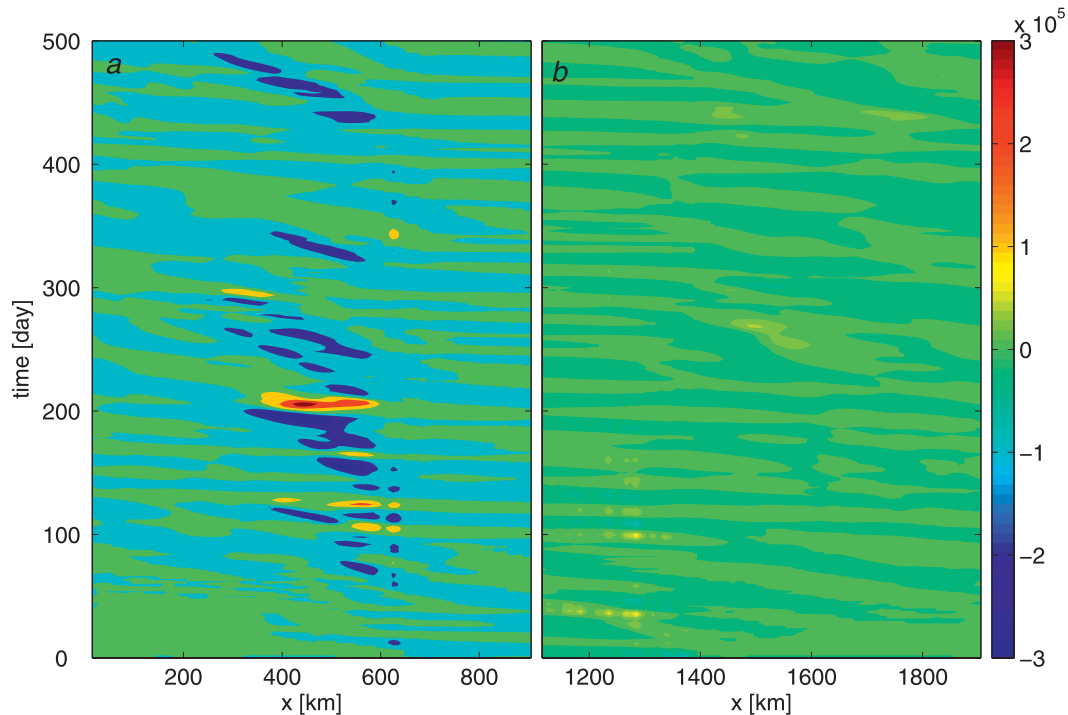
FIG. 14. The along-coast component of the tracer B flux (m^3 s^{-1}) in a subperiod in (a) the western half and (b) the eastern half of the bay.

the slope so that the advection of the topographic waves is relatively strong. The second way is related to the interaction between the coast and the topographic waves. Particles carried in this way follow a northwestward path. The interaction between a curved coast and topographic waves excited by a single eddy was found to be able to intensify the amplitudes of the waves and therefore the cross-shelf transport in both barotropic (Zhang 2009; Zhang et al. 2011) and baroclinic (Zhang 2009) situations. Generally speaking, the propagation of the topographic waves tends to be prevented by the coast in the narrow-shelf region, inducing the shortening of the wavelength, which further enhances the cross-isobath velocity as well as the wave amplitude. Compared with the barotropic case, the wave–coast interaction in the baroclinic single-eddy–topography interaction is much weaker because of the short decay length scale of the baroclinic eddy and dies out quickly as the forcing eddy leaves the coast with the topographic cyclone (Zhang 2009). However, in the current baroclinic model, the effect of the wave–coast interaction is significant because topographic waves are continuously excited by the offshore variability.

A typical wave–coast interaction event is displayed in Fig. 13 by four snapshots of the distribution of tracer B in one simulation. As the tracer is advected out of the bay toward the deep ocean by the offshore variability, the southern edge of the 0-concentration region withdraws more or less zonally uniformly seaward, whereas the northern edge of the 1-concentration region is pushed shoreward in a zonally asymmetric way. At day 680, the latter interface is located more to the north in the west of the bay, consisting of two seaward bumps: one is around $x = 750$ km and located farther north and the other is around $x = 1100$ km and located well inside the bay. Contours of lower tracer concentration near $x = 1000$ km are being stretched northeastward (denoted as E in Fig. 13) from day 680 to day 688, implying the existence of some deep-ocean variability near the slope edge. Meanwhile, the bump around the bay opening is advected westward by topographic waves and finally collapses onto the boundary around day 708. Along with that event, a big volume of the tracer-rich water is thrown out of the bay through its western edge. This is not a rare phenomenon in the simulation. Figure 14 shows the x–t plot of the along-coast component of the flux of tracer B in 500 days, in which strong, westward flux events occur with a frequency about once every 2 months near the western edge of the bay. In contrast, along the coast in the eastern half of the bay, the flux is much weaker, with no definite direction.

The wave–coast interaction enhances the cross-isobath motion near the western boundary and is therefore capable of driving water particles, which are originally
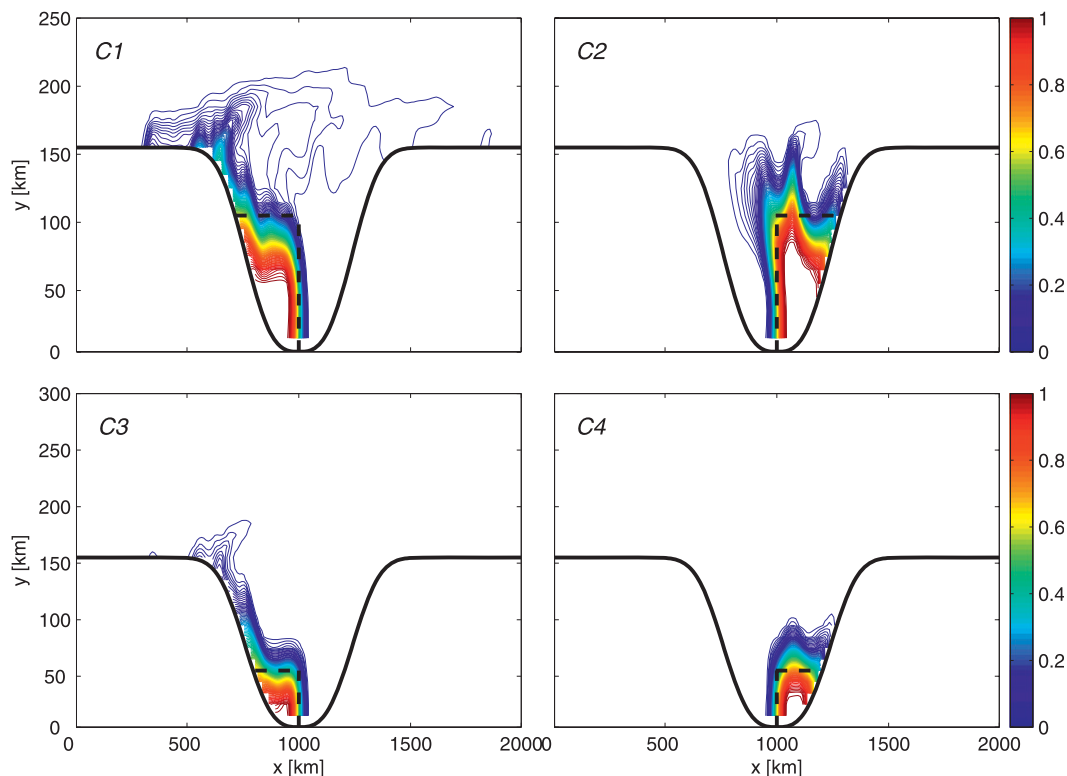
FIG. 15. The concentration distribution at the end of a subperiod of tracers C1, C2, C3, and C4.

located very far south, progressively toward the bay opening. This is a feature absent from the eastern boundary of the bay. Figure 15 shows the distributions of four tracers C1–C4 at the end of a subperiod. The four tracers are initially seeded with concentration 1 in areas bounded by the dark dashed line and the coast in Fig. 15 and 0 anywhere else. The concentration of C1 is initially 1 in the southwestern corner that extends northward from the tip of the bay to $y = 100$ km and eastward from the coast to the bay's middle longitude. The region of 1 concentration of tracer C2 is symmetric with that of tracer C1 about the middle longitudes. Initial distributions of tracers C3 and C4 are similar to those of C1 and C2, respectively, except that they cover a much smaller meridional range, from $y = 0$ to $y = 50$ km. By the end of the integration, there are remarkable differences between tracers initially distributed in the west and those in the east. A large amount of tracer C1 is advected along a northwestward path out of the bay, making the northwestern corner particularly high in tracer concentration. Once the bay water is carried onto the slope, it is more vulnerable to the offshore forcing, and the tracer contours over the slope show a tendency for the northeastward extension. Conversely, tracers C2 and C4 experience much less northward advection from their original locations because the local wave mechanism is not as strong as

that near the western boundary. This suggests that the water tends to be transported out of the bay more from the west than from the east, and the southeastern corner is a retention region for the cross-shelf exchange.

As suggested by Zhang (2009) and Zhang et al. (2011), topographic waves are greatly shortened and more inclined to break as they propagate from the wide shelf region into the narrower shelf region. In situations where the straight coast outside the bay is right aligned with the shelf edge as in case BAY, propagation of waves that are excited inside the bay is entirely blocked by the bay's western boundary, which causes strongest nonlinear wave–coast interactions as well as out-of-bay transport. Conversely, if the shelf width is larger than the depth of the bay or the shelf edge is to the north of the coast, waves can successfully propagate through the western corner without interacting with the coast and hence little out-of-bay transport is generated. On the other hand, if the first-layer slope is narrower and the bay is closer to the open ocean, waves excited near the bay are stronger and we expect greater wave–coast interactions.

c. Mean shelf circulation

The time-dependent motion at the bay's opening is the driving agent of the mean circulation within the bay. Because the bay is flat bottomed, contours of the surface
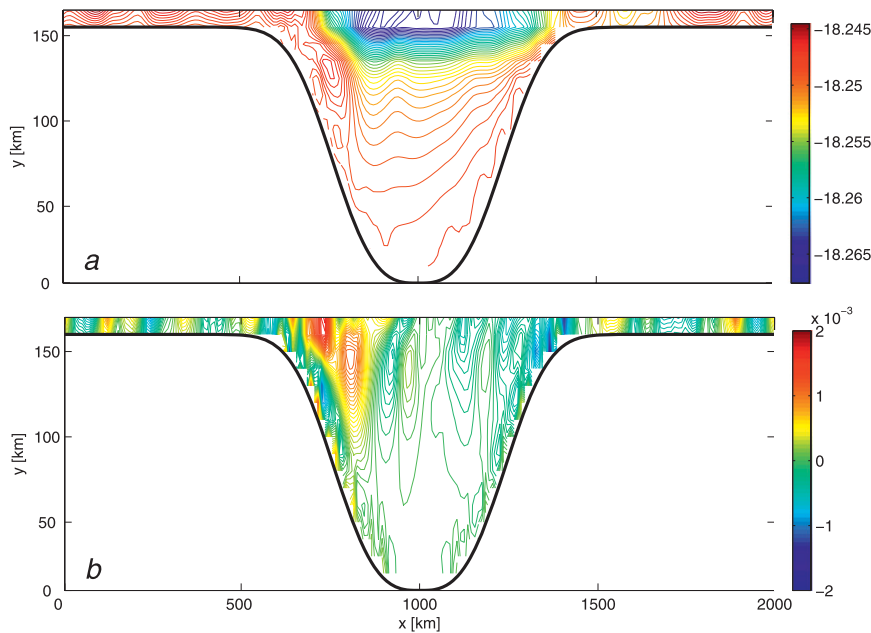
FIG. 16. (top) The mean surface elevation (m) within the bay in case BAY. (bottom) The mean meridional velocity (m s^{-1}) within the bay.

elevation can be taken as streamlines of the mean flow. As shown in Fig. 16a, most streamlines originating inside the bay cross the bay opening. The corresponding circulation is clockwise, flowing westward within the bay and eastward over the slope and decaying shoreward from the bay opening. The direction of the circulation is consistent with that observed over the WAP shelf, although its magnitude is rather weak, on the order of 10^{-3} m s^{-1}. The meridional flow (Fig. 16b) shows a zonally asymmetric feature: the northward flow is trapped within a fairly narrow region along the western boundary of the bay, whereas the shoreward returning flow is more widely distributed within the region to the east. To maintain the mass balance within the bay, the narrow outflow in the west is much stronger than the wide inflow in the interior. This feature reminds us of the similar character of the cross-shelf transport: the out-of-bay transport is intense near the western boundary because of the wave–coast interactions. This western intensification of the mean flow can be explained by the effect of the positive meridional PV gradient, similar to that of the planetary β effect, which induces the formation of the western boundary currents in oceanic basins. In the current situation, the β effect is due to not only the meridional variation of the Coriolis parameter but also the depth variation near the bay opening. If the topographic waves propagate eastward instead of westward, we would expect the intensification of both the transport and the mean circulation to take place along the eastern boundary of the bay.

5. Conclusions

This paper presents results of simulations of an ACC-like wind-driven zonal flow in a two-layer channel with different configurations of the bottom topography and the southern boundary. Interaction between the model ACC and a lower-layer "positive" (same sense as the interface slope) bottom slope is found to induce the formation of an additional zonal jet as well as a PV front over the sloping bottom in the upper ocean. The associated mechanism could explain the existence of the multiple jets in the ACC, or at least indicates the possible role of the bottom topography in strengthening the isopycnal slopes. Off the northeast coast of North America, the bottom topography slopes in the same way as the isopycnal does, and interactions between the topography and the deep-ocean eddies may affect the frontal structure observed along the shelf break.

The most important feature of the new, upper-layer PV front is that it exists between the main jet in the channel center and the shallow area near the southern boundary. As perturbed constantly by the main jet, this new front develops its own variability, which forces the sloping region in the south. A strong eddy–slope interaction occurs a couple of times a month, comparable to observations (Moffat et al. 2009). The volume transport across the first-layer slope edge driven by the offshore eddies is similar to the maximum Ekman transport in the channel.

In addition of driving the slope water directly down the topography, eddies generated from the new PV front

also excite topographic waves that propagate westward along the slope. These waves are essential in driving transport out of the bay and generating a clockwise mean circulation over the shelf, which are both intensified near the bay's western boundary by the wave–coast interaction that happens in the propagation direction of waves. The southeastern area of the bay is out of reach of the offshore eddies and has no wave–coast interactions, so water in that region is hardly exchanged with the outside.

The aforementioned results suggest the potential importance of the ACC–topography interaction in driving the onshore intrusion of the UCDW in the WAP region, but it is not clear whether the mechanism dominates the cross-slope transport. Factors such as the wind stress and topographic features over the shelf, which are both ignored in the current model, may also contribute to the exchange. For example, eddy structures may result from the interaction between the local wind-driven circulation and the topography, which in turn can produce the cross-isobath transport. In the absence of any depth variation in the along-slope (zonal) direction, the topographic waves tend to be blocked by the bay's western boundary, generating strong exchange in the nearby area. It is important to know how this picture is affected by the existence of topography along the slope such as Marguerite Trough, a deep trench between Adelaide and Alexander Islands, which is suggested by observations as a preferred site of the CDW intrusion (Moffat et al. 2009). All these issues await explorations with high-resolution models that incorporate influences from both the open ocean and the local topographies.

REFERENCES

Belkin, I. M., and A. L. Gordon, 1996: Southern Ocean fronts from the Greenwich meridian to Tasmania. *J. Geophys. Res.,* **101,** 3675–3696.

Berloff, P., I. Kamenkovich, and J. Pedlosky, 2009: A mechanism of formation of multiple zonal jets in the oceans. *J. Fluid Mech.,* **628,** 395–425.

Dinniman, M. S., and J. M. Klinck, 2004: A model study of circulation and cross-shelf exchange on the west Antarctic Peninsula continental shelf. *Deep-Sea Res. II,* **51,** 2003–2022.

——, ——, and W. O. Smith, 2011: A model study of Circumpolar Deep Water on the west Antarctic Peninsula and Ross Sea continental shelves. *Deep-Sea Res. II,* **58,** 1508–1523.

Frolov, S. A., G. G. Sutyrin, G. D. Rowe, and L. M. Rothstein, 2004: Loop Current eddy interaction with the western boundary in the Gulf of Mexico. *J. Phys. Oceanogr.,* **34,** 2223–2237.

Garfield, N., and D. L. Evans, 1987: Shelf water entrainment by Gulf Stream warm-core rings. *J. Geophys. Res.,* **92,** 13 003–13 012.

Hallberg, R., and P. Rhines, 1996: Buoyancy-driven circulation in an ocean basin with isopycnals intersecting the sloping boundary. *J. Phys. Oceanogr.,* **26,** 913–940.

——, and A. Gnanadesikan, 2006: The role of eddies in determining the structure and response of the wind-driven Southern Hemisphere overturning: Results from the Modeling Eddies in the Southern Ocean (MESO) project. *J. Phys. Oceanogr.,* **36,** 2232–2252.

Jacobs, S. S., 1991: On the nature and significance of the Antarctic Slope Front. *Mar. Chem.,* **35,** 9–24.

Josey, S. A., E. C. Kent, and P. K. Taylor, 1998: The Southampton Oceanography Centre (SOC) ocean-atmosphere heat, momentum and freshwater flux atlas. Southampton Oceanography Centre Rep. 6, 30 pp.

Karsten, R., and J. Marshall, 2002: Constructing the residual circulation of the ACC from observations. *J. Phys. Oceanogr.,* **32,** 3315–3327.

——, H. Jones, and J. Marshall, 2002: The role of eddy transfer in setting the stratification and transport of a circumpolar current. *J. Phys. Oceanogr.,* **32,** 39–54.

Lee, M. M., and A. Coward, 2003: Eddy mass transport in an eddy-permitting global ocean model. *Ocean Modell.,* **5,** 249–266.

McWilliams, J. C., W. R. Holland, and J. H. S. Chow, 1978: A description of numerical Antarctic circumpolar currents. *Dyn. Atmos. Oceans,* **2,** 213–291.

Moffat, C. F., B. Owens, and R. C. Beardsley, 2009: On the characteristics of Circumpolar Deep Water intrusions to the west Antarctic Peninsula continental shelf. *J. Geophys. Res.,* **114,** C05017, doi:10.1029/2008JC004955.

Munk, W. H., and E. Palmén, 1951: Note on the dynamics of the Antarctic Circumpolar Current. *Tellus,* **3,** 53–55.

Orsi, A. H., T. Whitworth, and W. D. Nowlin, 1995: On the meridional extent and fronts of the Antarctic Circumpolar Current. *Deep-Sea Res.,* **42,** 641–673.

Phillips, H. E., and S. R. Rintoul, 2000: Eddy variability and energetics from direct current measurements in the Antarctic Circumpolar Current south of Australia. *J. Phys. Oceanogr.,* **30,** 3050–3076.

Plumb, R. A., and R. Ferrari, 2005: Transformed Eulerian-mean theory. Part I: Nonquasigeostrophic theory for eddies on a zonal-mean flow. *J. Phys. Oceanogr.,* **35,** 165–174.

Rhines, P. B., 1975: Waves and turbulence on a beta-plane. *J. Fluid Mech.,* **69,** 417–443.

Sinha, B., and K. J. Richards, 1999: Jet structure and scaling in Southern Ocean models. *J. Phys. Oceanogr.,* **29,** 1143–1155.

Sutyrin, G. G., I. Ginis, and S. A. Frolov, 2001: Equilibration of baroclinic meanders and deep eddies in a Gulf Stream–type jet over a sloping bottom. *J. Phys. Oceanogr.,* **31,** 2049–2065.

Thompson, A. F., 2010: Jet formation and evolution in baroclinic turbulence with simple topography. *J. Phys. Oceanogr.,* **40,** 257–278.

Turner, J., T. A. Lachlan-Cope, S. Colwell, G. J. Marshall, and W. M. Connolley, 2006: Significant warming of the Antarctic winter troposphere. *Science,* **311,** 1914–1917.

Vallis, G. K., 2006: *Atmospheric and Oceanic Fluid Dynamics: Fundamentals and Large-Scale Circulation.* Cambridge University Press, 745 pp.

Wang, J., and M. Ikeda, 1997: Diagnosing ocean unstable baroclinic waves and meanders using quasigeostrophic equations and Q-vector method. *J. Phys. Oceanogr.,* **27,** 1158–1172.

Wang, X., 1992: Interaction of an eddy with a continental slope. Ph.D. thesis, Massachusetts Institute of Technology–Woods Hole Oceanographic Institution, 216 pp.

White, A. J., and N. R. McDonald, 2004: The motion of a point vortex near large-amplitude topography in a two-layer fluid. *J. Phys. Oceanogr.,* **34,** 2808–2824.

Whitworth, T. I., A. H. Orsi, S. J. Kim, W. D. Nowlin Jr., and R. A. Locarnini , 1998: Water masses and mixing near the Antarctic slope front. *Ocean, Ice, and Atmosphere: Interactions at the Antarctic Continental Margin,* S. S. Jacobs and R. F. Weiss, Eds., Antarctic Research Series, Vol. 75, Amer. Geophys. Union, 1–27.

Zhang, Y., 2009: Slope/shelf circulation and cross-slope/shelf transport out of a bay driven by eddies from the open ocean. Ph.D. thesis, Massachusetts Institute of Technology–Woods Hole Oceanographic Institution, 222 pp.

——, J. Pedlosky, and G. R. Flierl, 2011: Shelf circulation and cross-shelf transport out of bay driven by eddies from an open-ocean current. Part I: Interaction between a barotropic vortex and a steplike topography. *J. Phys. Oceanogr.,* **41,** 889–910.